

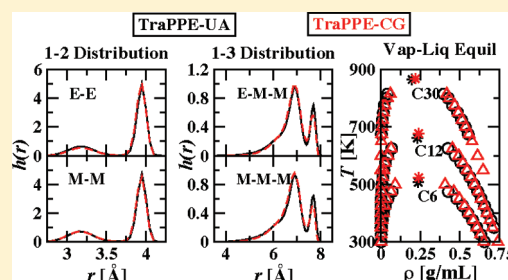
Transferable Potentials for Phase Equilibria—Coarse-Grain Description for Linear Alkanes

Katie A. Maerzke and J. Ilja Siepmann*

Departments of Chemistry and of Chemical Engineering and Materials Science, University of Minnesota, 207 Pleasant Street SE, Minneapolis, Minnesota 55455, United States

S Supporting Information

ABSTRACT: Coarse-grain potentials allow one to extend molecular simulations to length and time scales beyond those accessible to atomistic representations of the interacting system. Since the coarse-grain potentials remove a large number of interaction sites and, hence, a large number of degrees of freedom, it is generally assumed that coarse-grain potentials are not transferable to different systems or state points (temperature and pressure). Here we apply lessons learned from the parametrization of transferable atomistic potentials to develop a systematic procedure for the parametrization of transferable coarse-grain potentials. In particular, we apply an iterative Boltzmann optimization for the determination of the bonded interactions for coarse-grain beads belonging to the same molecule and separated by one or two coarse-grain bonds and parametrize the nonbonded interactions by fitting to the vapor–liquid coexistence curves computed for selected molecules represented by the TraPPE–UA (transferable potentials for phase equilibria–united atom) force field. This approach is tested here for linear alkanes where parameters for C_3H_7 end segments and for C_3H_6 middle segments of the TraPPE–CG (transferable potentials for phase equilibria–coarse grain) force field are determined and it is shown that these parameters yield quite accurate vapor–liquid equilibria for neat *n*-hexane to *n*-triacontane and for the binary mixture of *n*-hexane and *n*-hexatriacontane. In addition, the position of the first peak in various radial distribution functions and the coordination number for the first solvation shell are well reproduced by the TraPPE–CG force field, but the first peaks are too high and narrow.



1. INTRODUCTION

Despite tremendous gains in computational power over the past 50 years, atomistic simulations, where every atom (or united atom) is treated as an explicit interaction site, are not yet feasible for chemical systems with linear dimensions greater than 10 nm. The computational cost of any particle-based simulation increases as the number of interaction sites constituting the system of interest increases. This is mostly due to the relation between the number of distances that need to be computed to evaluate the system's energy or the forces acting on the particles, but for heterogeneous or microheterogeneous systems the cost also increases since particles have to translate over larger distances to explore the different spatial environments of the system. For simple pairwise additive potentials, the cost of the energy/force evaluation scales as M^2 (where M is the number of interaction sites) because a double loop over all interaction sites is involved. In the most favorable case, the cost of the energy/force evaluation scales as $M \ln M$ (commonly considered as linear scaling), which can be approached for very large systems with a linear dimension that greatly exceeds the distance used for the potential truncation.¹ Another factor contributing to the cost of particle-based simulations is the steepness of the potential energy surface, since rapidly changing energies (or large forces) require a small time step for molecular dynamics simulations or a small maximum displacement for Monte Carlo simulations. For

simulations of molecular systems, the steepest parts of the potential energy surface are usually associated with bond stretching modes, but special molecular dynamics or Monte Carlo algorithms can enhance the sampling of molecular systems.²

In a quest to extend molecular simulations to larger length and time scales, coarse-grain force fields have become increasingly popular over the past decade. Here the term coarse grain implies a systematic approach that reduces the number of degrees of freedom (or interaction sites) explicitly considered in the simulations while still maintaining the chemical specificity of the system. This is in contrast to simplified models (e.g., bead–spring polymer models) that are constructed to explore universal behavior of physical systems. However, one should note that, due to the scarcity of computational resources, early simulations treated entire molecules as a single interaction site (i.e., eliminating all intramolecular degrees of freedom),³ which was followed by pseudoatom models (treating a group of atoms, e.g., a methyl group, as a single interaction site),⁴ before all-atom models started to dominate.¹ Many coarse-grain models are built upon successful atomistic models, and multiscale simulations can be achieved by forward and reverse mapping procedures.^{5–9}

Received: July 10, 2010

Revised: February 13, 2011

Published: March 11, 2011

The fidelity of particle-based simulations depends on the accuracy of the force field and the precision of the sampling approach (that is, the efficiency of the simulation algorithm in exploring phase space and the availability of computational resources).¹⁰ To achieve accuracy and maintain chemical specificity, a judicious parametrization of the coarse-grain force field is essential (as it is also for all-atom or united-atom force fields). Since the coarse-graining process usually involves a reduction in the number of interaction sites, and concomitantly the number of degrees of freedom, the interaction potential between coarse-grained sites must to some extent mimic the energies/forces between a group of interaction sites in the parent fine-grain model. Necessarily, this implies that the coarse-grain potential represents the removed degrees of freedom in some average way. One way to achieve this is to treat the coarse-grain interactions as a potential of mean force that represents the ensemble-averaged free energy of the fine-grain model. In this case, the applicability of the coarse-grain force field is limited to the same thermodynamic conditions (i.e., temperature and pressure/density) used in the parametrization. However, in the same manner as for united-atom or all-atom force fields, one can also view the coarse-grain potential as an *effective* potential that is able to represent the interaction over a wider range of conditions (e.g., Lennard-Jones potentials are usually parametrized to represent both the pair and many-body interactions, fixed-charge models use an effective charge distribution, and united-atom models mimic entire CH_x groups). The latter view allows the development of models that are transferable over a range of thermodynamic conditions, but somewhat sacrifices accuracy at a specific condition.

In the past, coarse-grain force fields have been parametrized either to microscopic-level data obtained from simulations of a fine-grained model or to experimental (macroscopic) data. Perhaps the most popular approach for coarse-graining is the iterative Boltzmann inversion (IBI) procedure pioneered by Reith et al.¹¹ (this procedure is sometimes called RPM for the authors' names). The IBI approach is attractive due to a straightforward and generally applicable parametrization strategy that employs IBI to match the radial distribution function (RDF) for a coarse-grain model to the corresponding RDF obtained from an atomistic simulation or, in principle, scattering experiments.^{12,13} Although this iterative procedure can match the target RDF in a few iterations, it appears that this matching constrains mostly the shape but not necessarily the depth of the coarse-grain potential.¹¹ This should come as no surprise because the structure of a liquid is mostly determined by repulsive interactions,¹⁴ a fact that has been exploited successfully in perturbation theories of liquids.^{15,16} Jain et al.¹⁷ were able to recover the correct potential functions for single-site Lennard-Jones, Weeks–Chandler–Anderson, and square-well potentials. However, many iterations (over 1000) were required to converge to the correct potential, even though the RDF appeared well converged after only about 10 iterations. Modifying the procedure by including terms which consider the pressure and/or energy of the system reduced the number of iterations required for convergence to approximately 250.¹⁷ Chan et al.¹⁸ also found that many iterations (again approximately 250) were needed in order to converge a coarse-grain model for tethered nanoparticles that yields satisfactory aggregate distributions. Pressure and/or energy corrections can improve the performance of IBI potentials, as demonstrated by Hadley and McCabe for water¹⁹ and fatty acids.²⁰

Another popular coarse-graining approach based on microscopic-level information is the force matching procedure pioneered by Voth and co-workers.^{21–24} This approach has a sound statistical mechanical basis and relies on a variational procedure to match the forces (described by a linear combination of terms) acting on the coarse-grain model to those observed during individual configurations of a trajectory for the fine-grain model; i.e., it does not involve fitting to an ensemble averaged property such as the RDF.

Many other coarse-grain force fields use an analytic potential function, in much the same way as standard united-atom and all-atom force fields. These force fields are usually fit to thermodynamic, rather than structural, data. The MARTINI force field developed by Marrink et al.,²⁵ which uses a shifted Lennard-Jones (LJ) 12–6 potential, is designed for use in biomolecular simulations of lipids, surfactants, and proteins. The force field parameters were fit to reproduce the free energies of vaporization, hydration, and partitioning between water and organic phases at 300 K. Many different types of interactions sites were parametrized for the MARTINI force field, with a somewhat varying degree of success; e.g., it has been questioned whether the MARTINI water model yields a stable liquid phase at ambient conditions.^{26,27} However, largely due to the ability to simulate a wide variety of molecules, the MARTINI force field has proved quite popular. Recently, Chiu et al. have developed a force field similar to MARTINI for water and *n*-alkanes using a Morse potential.²⁸ This model was parametrized to the experimental heats of vaporization, bulk densities, and surface tensions at 298 K. While they obtain good agreement with these values, and also predict the free energies of transfer, diffusion coefficients, and isothermal compressibilities quite well, the model was not tested at any other temperatures.

Another popular coarse-grain force field for a large set of compounds has been developed by Klein and co-workers.^{29–32} Shelley et al.²⁹ developed a hybrid model for phospholipids, where the water and alkane parameters were fit to the bulk density and the other parameters were determined using an IBI procedure. This work was later expanded by Shinoda et al.³⁰ who screened different LJ $n-m$ potentials and found LJ 9–6 and 12–4 potentials suitable to reproduce experimental bulk densities and surface/interfacial tensions for water/surfactant systems at room temperature.

Also noteworthy are coarse-grain approaches pioneered for polymer systems that utilize density-dependent implicit solvent models^{33,34} or represent polymer–polymer interactions through density/compositions fields (i.e., removing the need to compute pair distances).^{35,36}

Although many of the coarse-grain force fields described above allow parameters to be transferred to different molecules, e.g., the same parameters are used for alkanes and the alkyl tails of alcohols or glycols, none of these force fields have been developed to be transferable over a wide range of thermodynamic conditions (temperature and pressure). A notable exception (and closely related in aim to the present work) are the coarse-grain models that have recently been developed by Mognetti et al.³⁷ to predict accurately the fluid phase equilibria for alkanes and some small solutes. Earlier, Liew and Mikami³⁸ obtained a soft attractive and repulsive potential that allows for much larger time steps in molecular dynamics simulations and reproduces both the vapor–liquid coexistence curve and the dynamic properties of Lennard-Jonesium.

A major goal of this research group has been the development of computationally efficient transferable force fields which

accurately predict a wide range of thermophysical properties. Up to now, the TraPPE force field has employed three levels of sophistication. For organic molecules, the simpler and more efficient representation, known as TraPPE–united atom (UA), represents CH_x groups (where $0 \leq x \leq 4$) as united atoms that interact via Lennard-Jones 12–6 and Coulombic potentials (the latter only for UA sites next to a polar group).^{39–42} The TraPPE–explicit hydrogen (EH) version^{43–45} is more accurate, but also more computationally expensive since the number of interaction sites increases by a factor of about 3. The polarizable version (TraPPE–pol) adds additional interaction sites, and both the partial charges and the Lennard-Jones parameters respond to changes in the environment.^{46,47} Although the TraPPE–UA force field has been successfully applied for the prediction of phase equilibria and other thermophysical properties of neat polymers and polymer–solvent mixtures,^{48–51} such simulations are extremely challenging and require large computational resources. Thus, a simple, transferable coarse-grain force field that reproduces many thermophysical properties over the entire stability range of fluid phases is highly desirable. Given that specific packing and electrostatic interactions are pivotal for crystalline phases,⁵² it is improbable that a coarse-grain force field would yield a satisfactory description of solid–fluid phase equilibria. However, one should ensure that the fluid range for the coarse-grain force field extends to the thermodynamic conditions of interest.³²

In the present work, the TraPPE family of force fields is extended to include TraPPE–coarse grain (CG) for linear alkanes. The general philosophy behind the development of the TraPPE force field is not only to predict a wide variety of thermophysical properties as accurately as possible, but also to minimize the number of different atom types in order to ensure the maximum amount of transferability. Parameters are in general fit to the smaller members of a homologous series and then transferred and validated for larger molecules and molecules with multiple functional groups. The remainder of this paper is organized as follows: the general features of the TraPPE–CG force field are briefly described in section 2. Sections 3, 4, and 5 describe the simulation details and the parametrization of the bonded and nonbonded interactions, respectively. Results for the vapor–liquid equilibria (VLE) of alkanes not included in the parametrization and for a binary mixture are presented in section 6. Section 7 provides a summary and an outlook toward extensions of the TraPPE–CG model.

2. MODEL

The development of the TraPPE–CG force field follows a somewhat different approach than previous coarse-graining procedures in the sense that we neither fit solely to microscopic properties of a parent fine-grain model nor to macroscopic experimental data. Instead, we use the TraPPE–UA model to generate pseudoexperimental data (saturated vapor and liquid densities, internal energy of vaporization, and transfer free energies) that are given the greatest weight during the parametrization, while also including intramolecular bead distributions, radial distribution functions, and the corresponding number integrals as secondary fitness evaluators. Use of the TraPPE–UA data is motivated by two observations: first, it would be widely optimistic to assume that one could parametrize a coarse-grain force field with similar accuracy as that found for the TraPPE–UA force field for a wide range of applications^{48,53–60}

and, hence, TraPPE–UA data can be used as a substitute for experimental data, allowing one to produce pseudoexperimental data for the desired systems and thermodynamic conditions. Second, fitting to TraPPE–UA data will be very beneficial in developing a coarse-grain force field that allows for seamless multiscale simulations (TraPPE–UA/CG) with efficient forward and reverse mapping procedures.

The TraPPE–CG force field (generally) maps a group of three interaction sites found in the TraPPE–UA force field onto a single CG bead. The 3:1 mapping is chosen here because (i) 3 UA beads often constitute a neutral group for polar molecules (e.g., alcohols and ethers,^{41,42}), (ii) the “bond” between directly connected CG beads represents 3 UA bonds, a length for which conformations can be generated very efficiently using concerted rotation Monte Carlo algorithms⁶¹ or fixed-end point configurational-bias Monte Carlo strategies,⁶² and (iii) it should lead to a gain in efficiency of about one order of magnitude.

The position of the CG bead is taken as the position of the central UA bead; that is, for a sequentially numbered n -hexane chain, the positions of the CG beads correspond to the positions of UA bead numbers 2 and 5. Choosing UA bead positions instead of the center of mass of the UA beads contained within each CG bead will facilitate a reverse mapping of CG beads to UA beads, but will likely sacrifice some accuracy over approaches that optimize the position of the CG bead.^{19,24}

In general, all interaction potentials of the TraPPE–CG force field are tabulated to allow for maximum flexibility (i.e., avoiding the restriction of simple analytical forms). This poses no problem for Monte Carlo simulations (with the exception of not allowing for the computation of the pressure via the virial formalism) but local spline fits with smoothing functions would be needed for molecular dynamics simulations. It should be noted here that the large number of coarse-grain force fields parametrized with the popular IBI procedure¹¹ also make use of tabulated numerical potentials. The entries in the tabulated potentials are spaced by 0.05 Å and linear interpolation using the two neighboring table entries is used to determine the potential for a given separation. [With this spacing and using linear interpolation, a tabulated UA potential reproduces the energy of the system calculated using an analytical function to within 0.1%.] For the convenience of implementing TraPPE–CG in molecular simulation programs that require potentials in analytical form, parameters for a sixth-order polynomial fit to the various bonded potentials are provided in the Supporting Information and those for the nonbonded interactions are provided in section 5. As indicated by explicit simulations, however, use of the analytical variant for the bonded interactions results in a loss of accuracy for longer alkanes.

The TraPPE–CG force field includes bonded and nonbonded terms. The former always include 1–2 interactions (“bond stretching”) and 1–3 interactions (“angle bending”) for CG beads belonging to the same molecule and separated by one or two CG bonds, respectively. In the TraPPE–CG force field, the 1–4 interactions (“dihedral rotation”) constitute an intermediate case that in some cases may require specific bonded potentials but in many other cases may be described well by the nonbonded potentials also used for intermolecular interactions. It should be noted that the 1–4 interactions for CG beads separated by three CG bonds correspond to interactions of triplets of UA sites separated by 7 to 11 chemical bonds. As also in atomistic force fields, intramolecular interactions of CG beads separated by four or more bonds are treated through the regular nonbonded potentials.

The nonbonded potentials are constructed in such a way that the interaction energy for pair distances greater than 14 Å (the value used for the spherical truncation of Lennard-Jones interactions in the TraPPE-UA force field) is set to zero. This choice of a shifted potential offers two main advantages: (i) it removes the need for tail corrections to the energy (and also pressure and chemical potential), an important point for CG force fields that are often used for heterogeneous systems; (ii) it simplifies the implementation for molecular dynamics algorithms and greatly reduces the influence of a switching function needed to set the forces to zero at the cutoff. Beyond matching the truncation distance of the TraPPE-UA force field, the choice of $r_{\text{cut}} = 14$ Å is motivated by the liquid structure of alkanes that often exhibits a second peak in the carbon-carbon radial distribution functions at $r \approx 10$ Å and a second minimum at $r \approx 12$ Å (see section 5) and by the fact that coarse-grain force fields are usually applied to systems with larger length scales than those amenable to atomistic models, i.e., $r_{\text{cut}} = 14$ Å is likely to be small relative to the typical simulation box length.

For the linear alkanes, we define two different interactions sites, one for the $\text{CH}_3\text{CH}_2\text{CH}_2$ end group (called CCC_E) and the other for the $\text{CH}_2\text{CH}_2\text{CH}_2$ groups in the middle of the molecule (called CCC_M). As will be seen in section 5, the interaction parameters differ significantly between CCC_E and CCC_M beads.

3. SIMULATION DETAILS

The MCCC-S-MN (Monte Carlo for Complex Chemical Systems-Minnesota) software program⁶³ developed by the Siepmann group was used for all simulations. Constant-temperature simulations using configurational-bias Monte Carlo strategies^{40,64–67} were carried out to probe the conformation of isolated molecules. These simulations used very brief equilibration periods followed by 10^7 Monte Carlo moves for the determination of conformational distributions.

Gibbs ensemble Monte Carlo^{68,69} (GEMC) simulations in the canonical (NVT) ensemble were carried out in order to compute the vapor-liquid coexistence curves (VLCCs), internal energies of vaporization, and free energies of transfer for single-component systems. In the canonical version of the Gibbs ensemble,⁶⁸ two separate periodic simulation boxes in thermodynamic contact, but without an explicit interface, are used. To equilibrate the chemical potential, molecules are swapped between the boxes with the aid of coupled-decoupled configurational-bias Monte Carlo (CBMC) algorithm.^{40,67} Volume exchanges are performed in order to equilibrate the pressure, and translational and rotational moves along with CBMC regrowths allow the system to reach thermal equilibrium. Simulations were also performed in the isobaric-isothermal (NpT) ensemble³ to compute liquid densities and radial distribution functions at 300 K. In addition, simulations for binary mixtures of *n*-hexane and *n*-hexatriacontane (C36) were performed in the NpT version of the Gibbs ensemble.⁶⁹

The system size for single-component systems consisted of 300 molecules, with the exception of *n*-triacontane (C30), where only 200 molecules were used. For the binary *n*-hexane/*n*-hexatriacontane mixture, the system size was increased to 600 molecules. Vapor-phase box sizes were adjusted so that on average at least 20 molecules were present in this phase. Volume moves were accepted on average once every 10 Monte Carlo (MC) cycles (1 MC cycle consists of N moves, where N is the number of molecules in the system). The fraction of swap moves was adjusted so that on average one swap move was accepted

every 10–30 MC cycles. The higher values are used at lower temperatures, where the acceptance rate of swap moves is generally much lower. Of the remaining moves, approximately 12% were CBMC regrowths, 25% were translations of individual CG beads, and the remainder were divided equally between translational and rotational moves of entire molecules. At every state point at least 150 000 MC cycles of equilibration were performed before starting the production runs. The production runs consisted of 250 000 MC cycles divided into five blocks in order to compute statistical uncertainties. For the binary mixture, four independent simulations were performed in order to get a more reliable estimate of the uncertainty. Calculated statistical uncertainties are given as the standard error of the mean.

The critical temperature (T_c) and density (ρ_c) were estimated using the scaling law⁷⁰

$$\rho_{\text{liq}} - \rho_{\text{vap}} = B(T - T_c)^{0.325} \quad (1)$$

and the law of rectilinear diameters⁷¹

$$\frac{1}{2}(\rho_{\text{liq}} + \rho_{\text{vap}}) = \rho_c + A(T - T_c) \quad (2)$$

where ρ_{liq} and ρ_{vap} are the saturated liquid and vapor densities, respectively. For all systems, only the five highest temperatures were used to determine the critical point. The internal energy of vaporization, U_{vap} , was computed from the difference of the molar energy of the vapor and liquid phases, and the Gibbs free energy of transfer from the liquid to the vapor phase was calculated according to^{72,73}

$$\Delta G_{\text{trans}} = -RT \ln \left(\frac{\rho_{\text{vap}}}{\rho_{\text{liq}}} \right) \quad (3)$$

4. PARAMETERIZATION OF BONDED INTERACTIONS

Bond stretching (1–2) potentials were parametrized using an iterative Boltzmann optimization procedure,¹¹ which we have modified to ensure transferability to multiple temperatures. Bond length distributions, $h(r_{12})$ (where r_{12} is the 1–2 separation of directly bonded beads), are first calculated for an isolated united-atom molecule at three temperatures (300, 400, and 500 K). The distributions are then used to calculate a tabulated potential, $u(r_{12})$, according to^{11,30}

$$u_0(r_{12}) = - \sum_{j=1}^3 \frac{1}{3} \left[k_B T_j \ln \left(\frac{h_j^{\text{UA}}(r_{12})}{(r_{12})^2} \right) + C_{0,j} \right] \quad (4)$$

where $T_j = 300, 400, \text{ and } 500$ K, h_j^{UA} is the TraPPE-UA distribution for the j th temperature, $C_{0,j}$ is a constant that shifts the potential for each temperature so that its global minimum has an energy of zero, and the division by $(r_{12})^2$ accounts for the Jacobian associated with a second bead being placed on the surface of a sphere centered on the first bead. Next, the distributions at all three temperatures are calculated using the current coarse-grain potential. This potential is then iteratively adjusted according to

$$u_{i+1}(r_{12}) = u_i(r_{12}) + \sum_{j=1}^3 \frac{1}{3} \left[k_B T_j \ln \left(\frac{h_{i,j}(r_{12})}{h_j^{\text{UA}}(r_{12})} \right) + C_{i,j} \right] \quad (5)$$

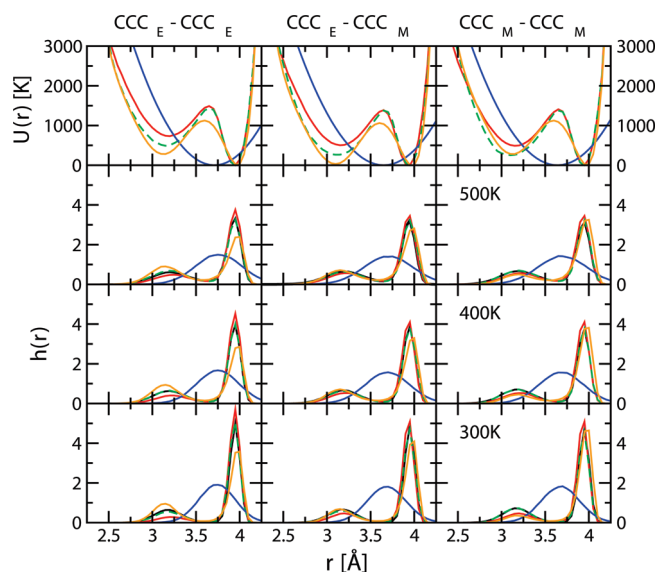


Figure 1. The 1–2 bond stretching potentials (top) and distributions for $\text{CCC}_E\text{--}\text{CCC}_E$ (left), $\text{CCC}_E\text{--}\text{CCC}_M$ (center), and $\text{CCC}_M\text{--}\text{CCC}_M$ (right) interactions at 300 (bottom), 400, and 500 K. The black line denotes the distributions obtained for the TraPPE-UA force field. The red, dashed green, orange, and blue lines denote the 1–2 potentials and corresponding distributions for the original inverted potentials, the iteratively optimized TraPPE-CG potentials, the sixth-order polynomial fits to the TraPPE-CG potentials, and the CG model by Shinoda et al.³⁰

where u_{i+1} and u_i are the new and current potentials and h_i is the current TraPPE-CG distribution. This procedure is repeated until the difference between the old and new potentials is less than 1% averaged over each bin with an energy less than 5000 $k_B K$. For the 1–2 bond stretching potentials, typically less than three iterations are required to adequately converge the potentials. A quadratic function is then used to locally smooth out the edges of the potential well where the sampling is not as good (and, hence, the distributions are noisier).

There are three types of 1–2 bond stretching potentials needed for linear alkanes: (i) for $\text{CCC}_E\text{--}\text{CCC}_E$ interactions that is fitted to TraPPE-UA *n*-hexane, (ii) for $\text{CCC}_E\text{--}\text{CCC}_M$ interactions that is fitted to TraPPE-UA *n*-nonane (concomitantly with the 1–3 $\text{CCC}_E\text{--}\text{CCC}_M\text{--}\text{CCC}_E$ interaction), and (iii) for $\text{CCC}_M\text{--}\text{CCC}_M$ interactions that is fitted to *n*-dodecane (concomitantly with the 1–3 $\text{CCC}_E\text{--}\text{CCC}_M\text{--}\text{CCC}_M$ interactions and using the nonbonded $\text{CCC}_E\text{--}\text{CCC}_E$ interactions obtained for *n*-hexane for the 1–4 intramolecular interactions). Upon examining the 1–2 bond stretching distributions in Figure 1, we can see that the iteratively optimized potentials reproduce the united-atom distributions quite well, whereas the original inverted potentials yield significant deviations for these distributions. For the linear alkanes, the higher peak in the distribution at $r = 3.9$ Å corresponds to the trans state of the single dihedral angle for carbon atoms separated by three bonds, the lower peak at $r = 3.2$ Å corresponds to the gauche state, and the minimum is caused by the trans–gauche barrier. Compared to atom–atom bond length distributions, the 1–2 CG distributions are very broad. A standard harmonic potential would not allow for two minima in the 1–2 potential and, hence, would not result in the two well-separated peaks observed in the distribution. It should be noted here that distributions with two maxima are also obtained when either the geometric center or the

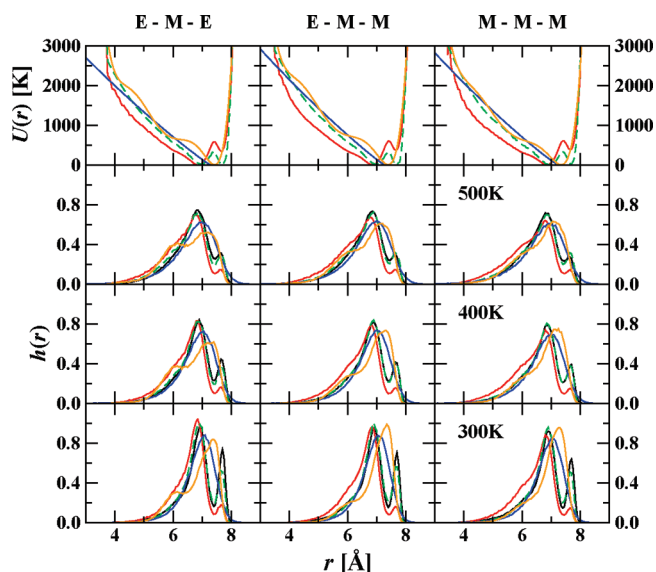


Figure 2. The 1–3 bond bending potentials (top) and distributions for $\text{CCC}_E\text{--}\text{CCC}_M\text{--}\text{CCC}_E$ (left), $\text{CCC}_E\text{--}\text{CCC}_M\text{--}\text{CCC}_M$ (center), and $\text{CCC}_M\text{--}\text{CCC}_M\text{--}\text{CCC}_M$ (right) interactions at 300 (bottom), 400, and 500 K. Colors as in Figure 1.

center of mass is used to define the location of the CG bead representing a group of three UA beads. Thus, the harmonic bond stretching potential found in many popular coarse-grain force fields^{25,30} may not be the best choice. For comparison, the harmonic potentials and the corresponding distributions obtained for the CG force field by Shinoda et al.³⁰ are also shown in Figure 1 (the MARTINI model uses a 4:1 mapping and cannot be compared directly). A sixth-order polynomial fit to the tabulated TraPPE-CG potential yields the double-peak feature, but the peak heights are not well reproduced. In this work, we did not attempt to further optimize the analytical form.

Given the broad 1–2 distributions for the CG model, it is clear that a regular angular dependent potential will not be able to represent the energetics of the 1–3 interactions; e.g., the same angle with two 1–2 bond lengths representative of the gauche state would yield a rather different 1–3 distance than one with two trans-state 1–2 bond lengths. Thus, we chose to express the 1–3 interactions via distance dependent potentials that were parametrized using the same procedure as for the 1–2 potentials. The 1–3 potentials require more iterations than the 1–2 potentials to converge, although the number of iterations is still quite small (less than 10). To fit the $\text{CCC}_E\text{--}\text{CCC}_M\text{--}\text{CCC}_E$, $\text{CCC}_E\text{--}\text{CCC}_M\text{--}\text{CCC}_M$, and $\text{CCC}_M\text{--}\text{CCC}_M\text{--}\text{CCC}_M$ potentials *n*-nonane, *n*-dodecane, and *n*-pentadecane were used, respectively, although the $\text{CCC}_E\text{--}\text{CCC}_M\text{--}\text{CCC}_M$ distributions for *n*-dodecane and *n*-pentadecane were indistinguishable. Again, the TraPPE-CG simulations for *n*-dodecane involve nonbonded $\text{CCC}_E\text{--}\text{CCC}_E$ interactions and those for *n*-pentadecane involve also nonbonded $\text{CCC}_E\text{--}\text{CCC}_M$ interactions that were determined from bulk simulations for *n*-dodecane (see section 5).

Figure 2 shows that the TraPPE-CG potentials accurately reproduce the TraPPE-UA distributions for all three 1–3 interactions found in the linear alkanes. The sharp peak at $r = 7.7$ Å that is most pronounced at low temperatures can be attributed to an all-trans conformation of the four C–C–C–C dihedral angles for carbon atoms separated by six C–C bonds.

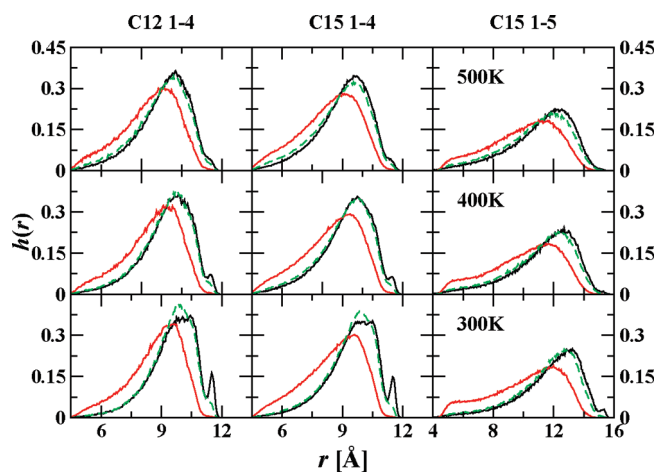


Figure 3. The 1–4 distributions for *n*-dodecane (left), and 1–4 and 1–5 distributions for *n*-pentadecane (center and right) at 300 (bottom), 400 (middle), and 500 K (top). Colors as in Figure 1.

The broad and asymmetric peak at $r \approx 6.9$ Å can be attributed to conformations with at least one dihedral in the gauche state. In this case, the sixth-order polynomial fit describes the overall shape of the 1–3 potentials reasonably well, but the distributions are significantly different with the main peak located near the minimum for the corresponding UA distribution, and the peak at smaller separations diminished to a shoulder. Similarly, a harmonic bond angle potential cannot yield a double-peaked distribution. The distributions obtained for the CG model by Shinoda et al.³⁰ are also shown in Figure 2 (to project the contribution of the angle bending potential for the 1–3 distance dependence, the equilibrium bond lengths are used for the top part of the figure, but the CBMC simulations used the angle bending potential) and, as expected, a single peak is found. Again, it should be noted that the double-peak feature in the 1–3 distributions is also found when the location of the CG bead is based on either the geometric center or the center of mass of the three UA beads (instead of the location of the central UA bead used for the TraPPE-CG force field).

To validate the transferability of the bonded potentials (in conjunction with nonbonded terms for intramolecular 1–4 interactions and beyond) to intramolecular distances that extend beyond the 1–3 distances (i.e., to check that the shape of longer linear alkanes is well represented), we calculated the 1–4 (end-to-end) distributions for *n*-dodecane and the 1–4 and 1–5 distributions for *n*-pentadecane using both the original inverted potentials and the iteratively optimized TraPPE–CG potentials. Although the original inverted potentials yield broader distributions with a maximum shifted to smaller distances and miss the minor peak/shoulder representative of all-trans 1–4 distances (UA carbon atoms separated by nine bonds), the TraPPE–CG potentials reproduce the TraPPE–UA results very well, albeit the fraction in the all-trans state is somewhat underestimated at the lower temperatures (see Figure 3).

To test how the TraPPE–CG model performs for even longer alkanes, we simulated a single *n*-triacontane (C30) chain and calculated the distributions for the end-to-end lengths, the 1–6 distances for CG beads 3 and 8 (the middle part of the molecule), and the 1–4 distances for CG end segments with middle segments (i.e., CG beads 1 and 4 or 10 and 7). Although the end-to-end and 1–6 distributions are not as accurate as the

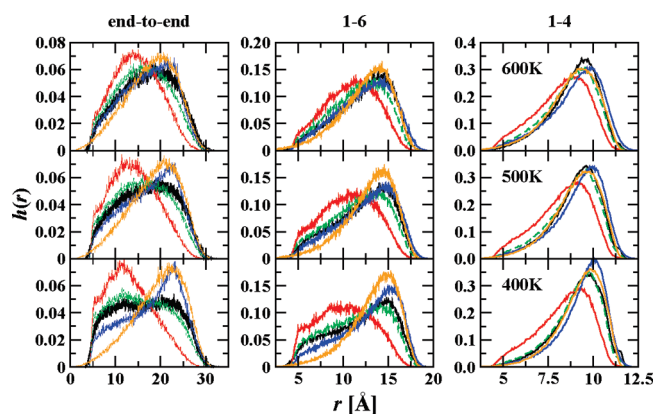


Figure 4. End-to-end (left), 1–6 (center), and 1–4 (right) distributions for *n*-triacontane at 400 (bottom), 500 (middle), and 600 K (top). Colors as in Figure 1.

distributions for smaller alkanes, TraPPE–CG with the iteratively optimized bonded potentials reproduces the TraPPE–UA distributions quite well (see Figure 4). In particular, it can reproduce the very broad end-to-end length distribution at $T = 400$ K where backfolding of the chain causes a significant propensity for close contacts. This justifies the omission of specific bonded potentials for the 1–4 interactions in linear alkanes. In contrast, the deviations for the original inverted potentials are now rather large. The 1–4 distributions for segments in the center of the molecule do not differ significantly from the 1–4 distributions shown in Figure 4. For comparison, the distributions obtained for TraPPE–CG with the sixth-order polynomial bonded potentials (in place of the tabulated potentials) and for the CG force field by Shinoda et al.³⁰ are also provided in Figure 4. On the positive side, these analytical potentials perform significantly better than the original inverted potentials. Nevertheless, these analytical representations are considerably less accurate than the iteratively optimized (tabulated) TraPPE–CG potentials. In particular, the analytical potentials yield 1–6 and end-to-end distributions with greatly reduced probabilities at shorter separations, i.e., the conformations are less globular.

5. PARAMETRIZATION OF NONBONDED INTERACTIONS

As mentioned in the Introduction, the iterative Boltzmann optimization procedure (or closely related variants) has been used to determine the nonbonded interactions of many coarse-grain force fields by fitting to selected radial distribution functions.^{11,18,20} In contrast, other coarse-grain force fields use analytical potentials for the nonbonded interactions.^{25,28,30} For this work, we extensively tested an iterative Boltzmann optimization that simultaneously targeted structural and thermodynamic properties for multiple temperatures (covering at least 100 K). However, the results proved unsatisfactory; i.e., when about equal weights were given to both types of properties, then neither was well reproduced, when the weight given to structural properties was increased, then the thermodynamic properties deteriorated, and vice versa when more weight was given to the thermodynamic properties. Thus, we decided to follow the TraPPE–UA parametrization approach and fit the nonbonded interactions to the vapor–liquid coexistence curves of small

molecules. It should be emphasized that this observation does not conflict with the finding by Jain et al.¹⁷ that the correct potential can be recovered after a sufficiently large number of iterations because in our case the CG mapping involves a reduction of the number of interaction sites by a factor of 3.

Based on previous experience,^{39,74–76} the vapor–liquid coexistence curve of a given compound can be used to determine uniquely only three independent force field parameters. Thus, although our implementation of the TraPPE–CG force field uses tabulated potentials, the fitting process explored parameters for analytic potentials that were used in tabulated form. We use tabulated potentials because we foresee the need for more flexible potential forms when the TraPPE–CG force field is extended to polar and hydrogen-bonding species. Some of the coarse-grain force fields³⁰ which use analytic nonbonded potentials, employ Lennard-Jones n – m potentials with attractive terms that do not scale as r^{-6} . In this case, the Lennard-Jones potential would contain four adjustable parameters. To assess whether $m \neq 6$ is appropriate to describe the dispersive interactions of two CG beads, we have investigated the distance scaling of the orientationally averaged interactions between two TraPPE–UA propane molecules (i.e., a simulation for two molecules using only rotational moves around the central bead was used to calculate the average interaction energy for a given temperature and separation). At all three temperatures investigated (300, 400, and 500 K), the interaction energy scales as r^{-6} for $r > 7$ Å, and the 3:1 coarse-graining does not change the order of the leading term in the dispersion energy.⁷⁷ Thus, the TraPPE–CG nonbonded potentials for the CCC_E and CCC_M beads were fit using the n , ϵ , and σ parameters for shifted LJ n –6 potentials given by

$$u_{\text{LJ}}(r_{ij}) = C\epsilon_{ij} \left[\left(\frac{\sigma_{ij}}{r_{ij}} \right)^n - \left(\frac{\sigma_{ij}}{r_{ij}} \right)^6 \right] - u_{\text{shift}} \quad (6)$$

where the constant C is determined using the fact that ϵ is the well depth and $u_{\text{LJ}}(\sigma) = 0$ for the *unshifted* potential. Since the potential is shifted to zero at the cutoff distance of 14 Å, u_{shift} is given by

$$u_{\text{shift}} = C\epsilon_{ij} \left[\left(\frac{\sigma_{ij}}{r_{\text{cut}}} \right)^n - \left(\frac{\sigma_{ij}}{r_{\text{cut}}} \right)^6 \right] \quad (7)$$

In a further effort to reduce parameter space, we decided to use the same value of n for the nonbonded interactions of the CCC_E and CCC_M beads and to employ the Lorentz–Berthelot combining rules⁷⁷ to determine the potential for unlike CCC_E–CCC_M pairs. As mentioned above, we foresee that the nonbonded potentials for CG beads representing polar or H-bonding groups may require more flexibility than offered by the LJ n –6 potential and, hence, simple combining rules are likely to fail in those cases.

Following the parametrization philosophy used for the TraPPE–UA force field,^{39–41} the CCC_E segment parameters were fit to n -hexane and the CCC_M segment parameters were then fit to n -dodecane. We chose to use n -dodecane rather than n -nonane for the fitting procedure since n -dodecane has an equal number of CCC_E and CCC_M segments (affording more sensitivity to the CCC_M parameters than n -nonane). TraPPE–CG parameters were fit to the saturated vapor and liquid densities of TraPPE–UA models at three temperatures covering a 100 K range surrounding the boiling point (300, 350, and 400 K for n -hexane; 450, 500, and 550 K for n -dodecane). While the critical properties were still considered in making the final

Table 1. Optimized Force Field Parameters for Nonbonded Interactions^a

n	C	CCC _E		CCC _M	
		σ (Å)	ϵ/k_B (K)	σ (Å)	ϵ/k_B (K)
12	4	4.64	285	4.51	264
11	4.55315	4.62	269	4.51	248
10	5.37914	4.61	254	—	—
9	6.75	4.60	236	—	—

^a Bold font indicates final TraPPE–CG parameters.

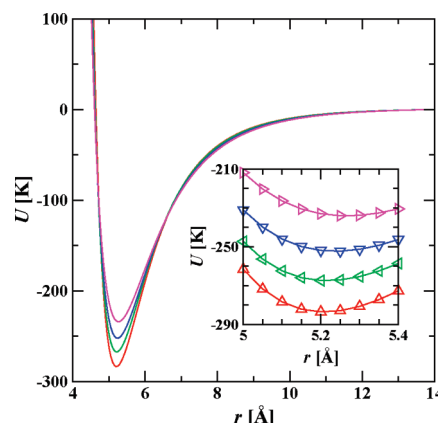


Figure 5. Comparison of the tabulated shifted LJ n –6 potentials for end segments. The red, green, blue, and magenta lines show the 12–6, 11–6, 10–6, and 9–6 potentials, respectively. The inset shows a close-up of the well region with the circles denoting the tabulated potential values and the lines showing the linear interpolation between table entries.

determination for parameter sets which reproduced the vapor and liquid densities in the 100 K range used for parameter fitting equally well, the critical properties were not included in the primary fitting procedure. This differs from the TraPPE–UA and TraPPE–EH force fields,^{39,43} where more weight is given to correctly predicting the critical point. However, in a coarse-grain model some concessions must be made. Rather than aim for accurate VLE data near the critical point, we focused instead on accurately predicting the saturated liquid and vapor densities at temperatures near the boiling point. Coarse-grain models are frequently used to simulate polymer melts, which are usually far from the critical point and much closer to the boiling point. Thus, we would like our model to be most accurate in the temperature range where it will most often be used.

For the CCC_E segment, we fit parameters for n -hexane using integer values of n ranging from 12 to 9 and the resulting parameters are summarized in Table 1. The LJ diameter for the CCC_E bead is found to decrease slightly from 4.64 Å for $n = 12$ to 4.60 Å for $n = 9$. In contrast, the decrease in the well depth with decreasing n is more dramatic (from 285 k_B K for $n = 12$ to 236 k_B K for $n = 9$). The tabulated potentials for CCC_E–CCC_E pair interactions are graphically depicted in Figure 5, where it can be seen that the differences in the well depths is compensated by the more attractive interactions at larger separations for the potentials with smaller n (all potentials intersect for $r \approx 6.7$ Å).

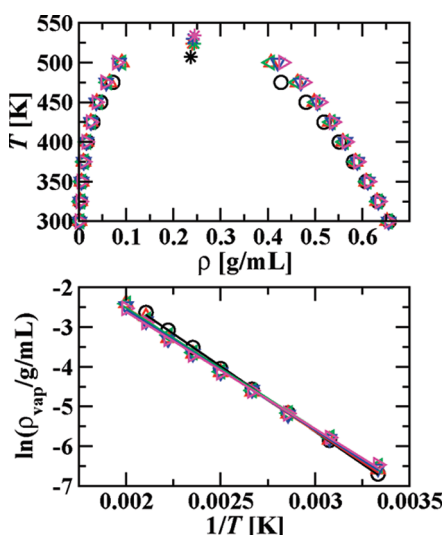


Figure 6. Comparison vapor–liquid coexistence curves and Clausius–Clapeyron plots for *n*-hexane: TraPPE–UA model (black circles), TraPPE–CG model using a shifted LJ 12–6 potential (red up triangles), and optimized CG models using shifted LJ 11–6, 10–6, and 9–6 potentials (green left triangles, blue down triangles, and magenta right triangles, respectively).

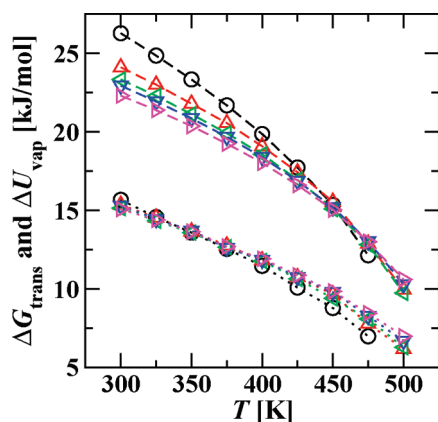


Figure 7. Comparison of transfer free energies and vaporization energies for *n*-hexane. Symbols and colors as in Figure 6.

As can be seen from the VLCCs in Figure 6, all models reproduce the saturated vapor and liquid densities at $T = 350$ K exceptionally well, but slightly overpredict ρ_{liq} at 400 K and ρ_{vap} at 300 K, whereas ρ_{liq} at 300 K and ρ_{vap} at 400 K are slightly underpredicted. Overall, the four models yield approximately the same degree of accuracy in the 300–400 K temperature range. However, when considering the VLCC data over the entire temperature range and the critical point, it becomes clear that the 12–6 and 11–6 LJ potentials yield results which are significantly more accurate than the 10–6 and 9–6 potentials; i.e., the former overpredict the critical temperature and underpredict the slope of the Clausius–Clapeyron plot (of ρ_{vap}) to smaller extents.

We also examined the Gibbs free energy of transfer and the internal energy of vaporization (see Figure 7). Given the accurate predictions of ρ_{liq} and ρ_{vap} over the temperature range used for the parametrization, it is not surprising that all four CG models predict the correct value of ΔG_{trans} at 350 K. However, at lower temperatures the CG models slightly underpredict the transfer

free energy, whereas at higher temperatures the transfer free energy is overpredicted and the errors become larger as the temperature increases. Again, the errors decrease for the potentials with increasing values of n . Compared to the results for ρ_{liq} , ρ_{vap} , and ΔG_{trans} , the deviations for ΔU_{vap} are much larger; i.e., compared to the TraPPE–UA data the CG models significantly underestimate ΔU_{vap} at low reduced temperatures (and, concomitantly, the entropy of vaporization since $T\Delta S_{\text{vap}} = \Delta H_{\text{vap}}$). Clearly, the 3:1 reduction in the number of interaction sites during the coarse-graining affects the magnitudes of the enthalpic and entropic contributions, whereas ΔG_{trans} can be reproduced quite well. This comes as no surprise since similar observations have been made from comparisons of united-atom alkane models with interaction sites placed on the carbon positions to experimental data,³⁹ whereas force fields that use exp–6 potentials,⁷⁴ anisotropically displaced interaction sites,⁷⁵ or additional interaction sites placed on the C–H bond centers⁴³ have been shown to yield accurate vapor pressures and enthalpies of vaporization for linear alkanes.

After the CCC_E bead parameters were obtained, the remaining CCC_M bead parameters were fit to *n*-dodecane. For the CCC_M segment we only considered the cases where $n = 11$ or 12, since smaller values of n yielded unsatisfactory results for *n*-hexane. The CCC_M segment parameters can be found in Table 1. Upon examining the vapor–liquid coexistence curve and Clausius–Clapeyron plot (see Figure 8), we find very little difference between the 11–6 and 12–6 potentials. Both predict slightly too high ρ_{liq} at high temperatures (resulting in a critical temperature that is too high) and ρ_{vap} at low temperatures, whereas they slightly underpredict ρ_{liq} at low temperatures and ρ_{vap} at high temperatures. Although both potentials yield very good results, the 12–6 potential is again slightly more accurate (as also indicated by smaller deviations for T_c and the slope of the Clausius–Clapeyron line). As can be seen in Figure 9, ΔG_{trans} for *n*-dodecane is well reproduced by both the 12–6 and 11–6 potentials, with only a small underprediction at low temperatures and a very slight overprediction at high temperatures. The differences in ΔU_{vap} are again larger than those for ΔG_{trans} , and the 12–6 potential yields significantly better predictions for the former. Comparing the ϵ and σ parameters for the CCC_E and CCC_M beads, we note that the relative differences are much smaller than for the methyl and methylene beads of the TraPPE–UA force field (as should be expected because of the greater similarity of propyl and a propylene segments) and are quite close to those used in the CG force field by Shinoda et al.³⁰ ($\sigma_{\text{CCC}_E}/\sigma_{\text{CCC}_M} = 1.03$ versus $\sigma_{\text{CT}}/\sigma_{\text{CM}} = 1.02$; $\epsilon_{\text{CCC}_E}/\epsilon_{\text{CCC}_M} = 1.08$ versus $\epsilon_{\text{CT}}/\epsilon_{\text{CM}} = 1.12$).

The VLE properties of *n*-dodecane described by the CG force field of Shinoda et al.³⁰ and the MARTINI force field²⁵ are also shown in Figures 8 and 9. Albeit not as accurate as the TraPPE–CG force field, both models yield remarkably good predictions for the VLE properties (with the exception of the saturated liquid density for the MARTINI force field) and are more accurate than some united-atom and explicit-hydrogen force fields.^{78,79} This may be attributed to the inclusion of the free energy of vaporization and the surface tension in the parametrization of the MARTINI and Shinoda et al. force fields, respectively. For the relatively short *n*-dodecane molecule, the TraPPE–CG variant with analytical bonded and nonbonded potentials closely reproduces the VLE properties for the TraPPE–CG model with tabulated potentials.

Based on the VLE properties for both *n*-hexane and *n*-dodecane, it is clear that the LJ 12–6 potentials yield the best

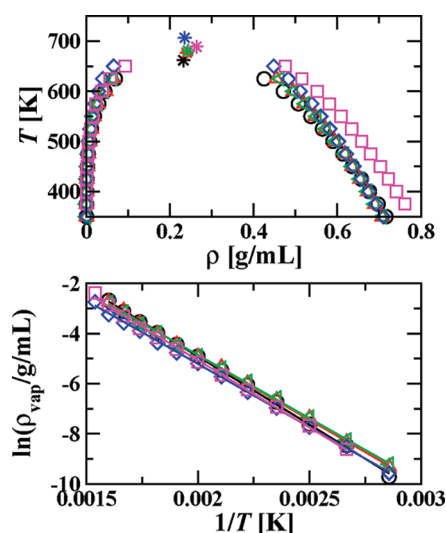


Figure 8. Comparison of vapor–liquid coexistence curves and Clausius–Clapeyron plots for *n*-dodecane: TraPPE–UA model (black circles), TraPPE–CG model using a shifted LJ 12–6 potential (red up triangles), optimized CG model using a shifted LJ 11–6 potential (green left triangles), CG force field by Shinoda et al.³⁰ (blue diamonds), and MARTINI force field²⁵ (magenta squares).

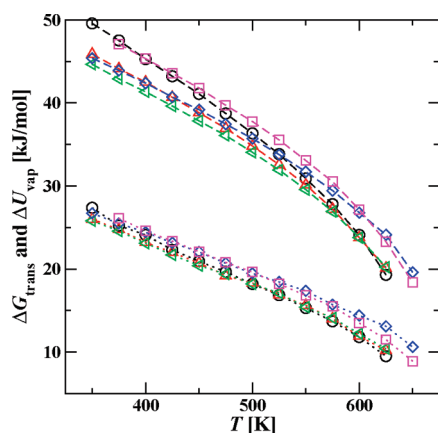


Figure 9. Comparison of transfer free energies and vaporization energies for *n*-dodecane. Symbols and colors as in Figure 8.

predictions, with mean unsigned percentage errors (MUPEs) of 2%, 11%, 3%, and 5% for ρ_{liq} , ρ_{vap} , ΔG_{trans} , and ΔU_{vap} over the entire temperature range for both molecules (the MUPEs are about a factor of 2 smaller when only the temperature range used in the parametrization are considered). Furthermore, the prediction of the VLE data appears to improve as the inverse power of the repulsive term is increased. This is consistent with the recent observations by Potoff and Bernard-Brunel⁷⁶ that larger values of n lead to better predictions of the saturated vapor pressures for united-atom perfluoroalkane models. In this work, values of n larger than 12 were not considered because (i) the repulsive term of the CG force field should not be steeper than that of the parent UA force field, (ii) steeper repulsive terms would necessitate a shorter time step for molecular dynamics simulations, and (iii) most importantly, steeper potentials lead to steadily worse description of the liquid structure (see below).

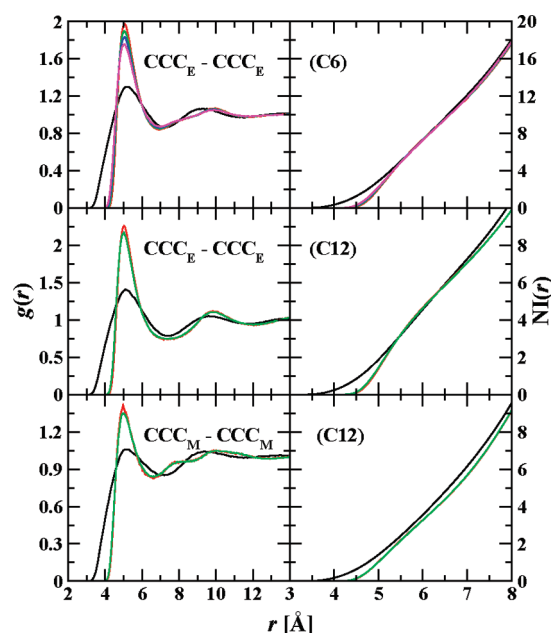


Figure 10. Radial distribution functions (left) and number integrals (right) for $\text{CCC}_E\text{--}\text{CCC}_E$ pairs in *n*-hexane (top), $\text{CCC}_E\text{--}\text{CCC}_E$ pairs in *n*-dodecane (middle), and $\text{CCC}_M\text{--}\text{CCC}_M$ pairs in *n*-dodecane (bottom). The black, red, green, blue, and magenta lines represent data for the TraPPE–UA model, the TraPPE–CG model using a shifted LJ 12–6 potential, and optimized CG models using shifted LJ 11–6, 10–6, and 9–6 potentials, respectively.

We assessed the ability of the coarse-grain potentials to reproduce structural properties by calculating radial distribution functions (RDFs) for *n*-hexane and *n*-dodecane and comparing to the corresponding UA RDFs (this is a direct comparison because the location of the CG beads represent those of specific UA sites). As can be seen from Figure 10, the CG $\text{CCC}_E\text{--}\text{CCC}_E$ and $\text{CCC}_M\text{--}\text{CCC}_M$ RDFs for all values of n are overstructured relative to the UA RDFs. As already alluded to earlier, our experience shows that it is likely not possible to find a CG potential that reproduces both thermodynamic and structural properties over a wide range of state points and, hence, a compromise must be made. Although many coarse-grain models place a great deal of weight on obtaining accurate RDFs,^{11,18–20} other coarse-grain models fit to thermodynamic (rather than structural) data also yield overstructured RDFs.^{28,80} Thus, we conclude that a coarse-grain model can either reproduce thermodynamic or structural properties to a high degree of accuracy. Since the focus of the TraPPE force field is on accurately predicting phase equilibria, solubilities, and related properties, we have chosen VLE data as the primary parametrization target and use structural data only as a secondary target. Taking a closer look at Figure 10, we see that the CG potentials with softer repulsive terms (smaller values of n) produce somewhat better RDFs than the potentials with larger values of n . However, this slight improvement in the RDFs does not compensate for the less satisfactory performance of the 9–6 potential in predicting the vapor–liquid coexistence densities. From the RDFs it is also evident that much softer potentials ($n < 9$) would be required to yield satisfactory RDFs. On the positive side, the TraPPE–CG force field accurately reproduces (i) the location of the first peak in the RDFs, (ii) the trend in the heights of the first peak (e.g., the value for the $\text{CCC}_E\text{--}\text{CCC}_E$ peak of

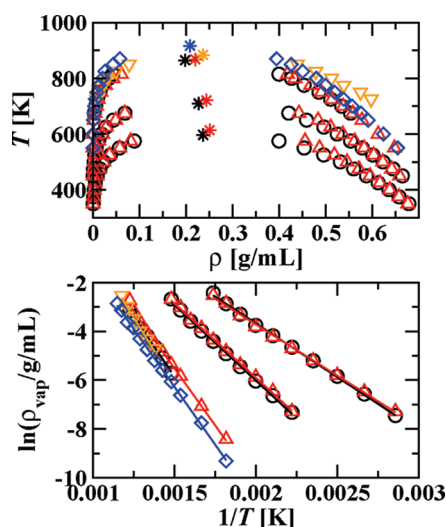


Figure 11. Comparison vapor–liquid coexistence curves and Clausius–Clapeyron plots for *n*-nonane, *n*-pentadecane, and *n*-triacontane: TraPPE–UA model (black circles), TraPPE–CG model (red up triangles), TraPPE–CG variant using analytical bonded and nonbonded potentials (orange down triangles), and CG force field by Shinoda et al.³⁰ (blue diamonds).

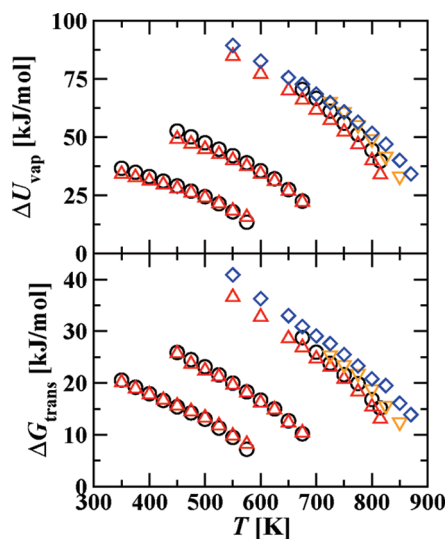


Figure 12. Comparison of transfer free energies and vaporization energies for *n*-nonane, *n*-pentadecane, and *n*-triacontane. Symbols and colors as in Figure 11.

n-dodecane is about 10% higher than that for *n*-hexane), and (iii) the coordination numbers for the first solvation shell. In particular, the latter quantity may be more important for solvation thermodynamics than the peak shape, which is too narrow for TraPPE–CG.

Overall, we judge that the tabulated potentials based on the shifted LJ 12–6 potentials best satisfy our objectives for a transferable force field, and, hence, they are selected for the nonbonded interactions in the TraPPE–CG force field. Comparison of the parameters for the CCC_E and CCC_M segments shows a 3% larger LJ diameter and an 8% larger LJ well depth for the CCC_E bead than for the CCC_M bead (see Table 1), i.e., the differences are significant and justify the use

Table 2. Critical Temperature, Critical Density, and Liquid Density at 300 K for TraPPE–UA and TraPPE–CG^a

molecule	force field	T_c (K)	ρ_c (g/mL)	ρ_{liq} (g/mL)
<i>n</i> -hexane	UA	507 ₂	0.237 ₂	0.6566 ₃
	CG	525 ₂	0.240 ₂	0.6526 ₃
<i>n</i> -nonane	UA	597 ₂	0.237 ₃	0.7194 ₁
	CG	614 ₂	0.251 ₃	0.7134 ₄
<i>n</i> -dodecane	UA	662 ₂	0.232 ₃	0.7527 ₄
	CG	667 ₃	0.240 ₃	0.7419 ₄
<i>n</i> -pentadecane	UA	710 ₂	0.227 ₂	0.7737 ₂
	CG	721 ₂	0.244 ₂	0.7599 ₅
<i>n</i> -triacontane	UA ⁸¹	865 ₂	0.198 ₃	—
	CG	867 ₃	0.219 ₄	—

^a Subscripts indicate uncertainties in the final digit.

of these different groups versus representing both with a single set of parameters.

6. VALIDATION

6.1. Transferability to Other Linear Alkanes. To test the transferability of the new CCC_E and CCC_M segment parameters, we investigated the VLE properties of *n*-nonane, *n*-pentadecane, and *n*-triacontane (see Figures 11 and 12). The TraPPE–CG force field reproduces very satisfactorily the saturated vapor and liquid densities (and correspondingly also the transfer free energies) of the TraPPE–UA model for *n*-nonane and *n*-pentadecane. As also observed for the parametrization compounds (*n*-hexane and *n*-dodecane), the TraPPE–CG model slightly overestimates the vapor densities at low reduced temperatures and the liquid densities at high reduced temperatures. Again, the internal energies of vaporization are somewhat underpredicted over the entire temperature range. For *n*-triacontane, the deviations in ρ_{vap} and ΔG_{trans} are larger, but the predictions are still rather satisfactory considering that the VLE data were obtained at temperatures much higher than those used in the parametrization for the shorter alkanes.

Averaged over all five alkanes (from *n*-hexane to *n*-triacontane) and all temperatures, the MUPEs (TraPPE–CG versus TraPPE–UA) in ρ_{liq} , ρ_{vap} , ΔG_{trans} , and ΔU_{vap} are 2%, 13%, 4%, and 6%, i.e., outstanding transferability for a coarse-grain force field. Data for the critical temperature, critical density, and liquid density at 300 K and 1 atm are listed in Table 2. In general, the TraPPE–CG model overpredicts the critical temperature by 2% and the critical density by 6%, whereas the liquid density at ambient conditions is slightly underpredicted (by 1%). Interestingly, the TraPPE–CG force field also yields a maximum in the critical density for *n*-nonane, in good agreement with experimental measurements and simulation data for atomistic models.^{82,83}

VLE properties for *n*-triacontane computed with the analytical variant of the TraPPE–CG force field and the CG force field by Shinoda et al.³⁰ are also included in Figures 11 and 12. Although the former can closely match the VLE properties of the tabulated form for *n*-dodecane, the differences for *n*-triacontane are very significant (particularly for the saturated liquid density). Given that the analytical and tabulated forms of the nonbonded potentials are nearly indistinguishable, the differences must be due to the bonded potentials. Since the analytical form of the

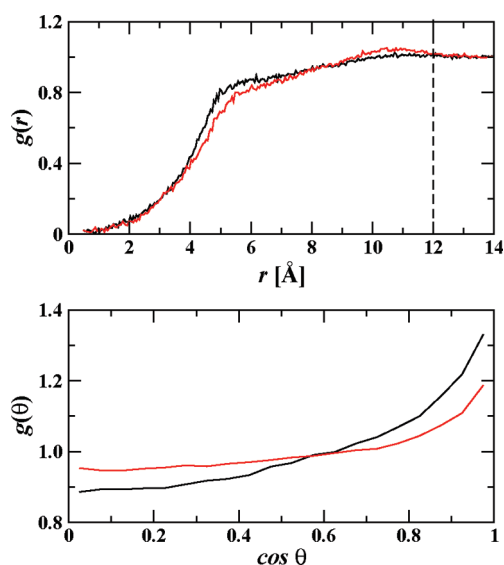


Figure 13. Comparison of the center-of-mass radial distribution functions and the distributions of mutual orientations for *n*-pentadecane at ambient conditions: TraPPE-UA model (black lines) and TraPPE-CG model (red lines).

bonded interactions yields more elongated (less globular) chain conformations than the tabulated form (see Figure 4), it is surmised that the less globular chains can pack better in the condensed phase leading to an enhanced density. Simulations at $T \leq 700$ K for the analytical variant exhibit a break in the slope of the Clausius–Clapeyron plot and the vaporization energies, indicating the possibility of a phase transition to a more ordered phase. Thus, use of a sixth-order polynomial fit for the bonded potentials comes with some loss of accuracy and use of local spline fits may be preferable to convert the tabulated potentials into continuous potentials. For the CG force field by Shinoda et al.,³⁰ the saturated liquid densities are only slightly overestimated but the critical temperature is significantly overestimated. These deviations may be caused by the preference for slightly less globular conformations (but closer to the benchmark data than for the analytical form of the TraPPE-CG bonded potentials, see Figure 4)) and a slightly too attractive nonbonded potential for the middle segment.

As mentioned in section 1, it is also important to validate that the VLE range and the stability of the liquid phase extend to sufficiently low reduced temperatures to cover regions of interest, e.g., ambient temperatures. In our case, the isobaric–isothermal ensemble simulations for *n*-pentadecane at 300 K and 1 atm are close to the experimental triple point. Furthermore, the TraPPE-CG force field yields enhanced first peaks in the liquid-phase RDFs, and it is possible that the entropy of fusion is smaller for a coarse-grain model due to the reduced number of conformational degrees of freedom. Thus, we have further analyzed the structure of the *n*-pentadecane liquid at ambient conditions. As can be seen in Figure 13, the TraPPE-CG model reproduces closely the center-of-mass RDF of the TraPPE-UA model. Neither of them exhibits the features expected to appear upon solidification; i.e., they do not show a strong peak at $r \approx 5$ Å as found in crystalline phases, and the pronounced extension of the RDFs to short separations indicates significant entanglement. Since the RDFs do not yield a clear peak, we have used $r = 12$ Å to define the boundary of the first and second solvation shells

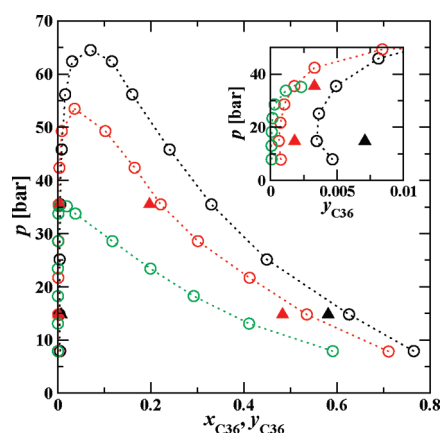


Figure 14. Pressure–composition diagram for the *n*-hexatriacontane/*n*-hexane mixture at 621.8 (black) 573.1 (red), and 521.7 K (green). Experimental data⁸⁵ and TraPPE-CG predictions are shown as open circles and filled triangles, respectively. The inset shows a close-up of the vapor-phase compositions. Note that the dotted lines are merely included to help guide the eye and do not represent experimental data.

around a given molecule. A comparison of the mutual orientations of molecules within the first solvation shell demonstrates a rather weak preference for parallel alignments. Based on these structural measures, it is very likely that the TraPPE-CG model yields a liquid phase for *n*-pentadecane that is stable at ambient conditions.

6.2. Transferability to a Binary Mixture. Mixtures of long and short hydrocarbons are frequently encountered in the petrochemical industry and in polymer synthesis and processing. Thus, knowledge of their liquid–liquid and vapor–liquid phase behavior is important for these applications and has been extensively studied by experiment, molecular-based equations of state, and molecular simulation.^{84–90} As a model polymer–(solvent and/or monomer) system, we have examined the pressure–composition diagram of a mixture of supercritical *n*-hexane with *n*-hexatriacontane (C36), where *n*-hexatriacontane is considered a mimic for polyethylene. In this case, we are comparing to experimental data⁸⁵ instead of TraPPE-UA since the UA simulations, while not impossible, would be quite challenging. Although the experimental measurements were performed at three different temperatures and seven or eight pressures, we have only simulated three state points: 573.1 K at 14.80 and 35.49 bar and 621.8 K at 14.80 bar. These three points are enough to allow us to determine whether TraPPE-CG predicts the correct temperature and pressure dependence of the composition. We did not perform simulations at the lowest experimental temperature (521.7 K) because TraPPE-CG *n*-hexane is not supercritical at this temperature.

Examination of the phase diagram presented in Figure 14 reveals that the TraPPE-CG force field predicts the correct trends for the pressure and temperature dependence of the composition, i.e., an increase of the swelling (increase of x_{C36}) for the high-density phase with decreasing temperature or increasing pressure and an increase of the C36 solubility in the low-density phase with increasing temperature or pressure (only for the pressure range investigated here). The coexistence region is somewhat narrower for the TraPPE-CG data than found experimentally.⁸⁵ This deviation is likely caused by the overprediction of *n*-hexane's critical temperature by the TraPPE-CG force field, i.e., an absolute temperature of 573.1 K corresponds

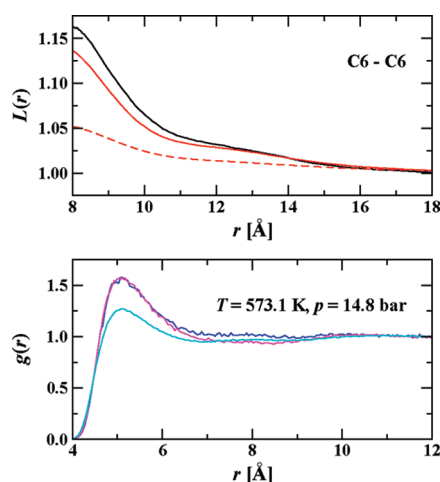


Figure 15. Local mole fraction enhancements (top) and radial distribution functions (bottom) for the *n*-hexatriacontane/*n*-hexane mixture. The solid black, solid red, and dashed red lines depict the C6–C6 local mole fraction enhancement at 621.8 K/14.8 bar, 573.1 K/14.8 bar, and 573.1 K/35.5 bar, respectively. The blue, magenta, and cyan lines depict the bead–bead radial distribution functions for C6/CCC_E–C6/CCC_E, C6/CCC_E–C36/CCC_E, and C6/CCC_E–C36/CCC_M, respectively, at 573.1 K/14.8 bar.

to a reduced temperature of 1.129 for the experimental system, whereas it corresponds only to $T^* \approx 1.09$ for the TraPPE–CG model (or, a simulation temperature of 593 K would be needed to be at the same T^* as the experimental measurements at 573.1 K). In addition, we found that ρ_{vap} is overpredicted for *n*-triacontane (see Figure 11), and a similar trend is likely to be observed for C36.

Some structural analysis of the high-density phase for this binary mixture is presented in Figure 15. The phase diagram shows significant swelling of this phase by *n*-hexane and computation of the local mole fraction enhancement ($L(r)$, the ratio of the C6–C6 number integral over the sum of the C6–C6 and C6–C36 number integrals normalized by the bulk mole fraction, all based on the center-of-mass positions⁴¹) allows us to probe whether the phase exhibits microheterogeneity. The fact that $L(r)$ is larger than unity at short separations indicates a local enhancement of the composition, i.e., there is a slight preference for C6 molecules to be surrounded by other C6 molecules. The magnitude of this enhancement is quite small, as should be expected for a mixture of two nonpolar compounds, and decreases with increasing x_{C6} , i.e., when more *n*-hexane is present then the composition is less heterogeneous. Also shown in Figure 15 are selected RDFs for the mixture with $x_{\text{C6}} \approx 0.5$. As can be seen, there is a slight preference for *n*-hexane's CCC_E beads to have other CCC_E beads in the first solvation shell, with very little difference between solvation by CCC_E belonging to C6 or C36. Similar behavior has been observed for other polymer–monomer mixtures.⁸⁹

7. CONCLUSIONS

The TraPPE–CG force field for linear alkanes accurately reproduces the saturated liquid and vapor densities and transfer free energies obtained for the TraPPE–UA force field over the entire vapor–liquid coexistence curve. In addition, the position of the first peak in the radial distribution functions and the coordination number in the first coordination shell are well

reproduced. However, the first peak is narrower and higher for the TraPPE–CG force field. Furthermore, the magnitude of the internal energy of transfer and correspondingly also of the entropy of transfer are somewhat too small. The latter is not unexpected because a similar observation was made previously when comparing TraPPE–UA to TraPPE–EH. The transferability of the TraPPE–CG force field is illustrated through computation of the vapor–liquid phase equilibria for linear alkanes not included in the parametrization and for the binary mixture of *n*-hexane and *n*-hexatriacontane. Thus, for the homologous series of linear alkanes for which the attractive nonbonded interactions are dominated by dispersion forces, it is possible to develop a coarse-grain force field that reduces the number of interaction sites by a factor of 3 compared to the parent united-atom force field.

In the future, we plan to apply the parametrization philosophy described here to develop compatible coarse-grain models for ethers and alcohols, i.e., extensions that requires the coarse-grain model to describe accurately dipole–dipole and hydrogen-bonding interactions. It is likely that these extensions will necessitate departures from LJ 12–6 potentials and simple combining rules and utilize the full flexibility of tabulated potentials. This flexibility was exploited here for the bonded 1–2 and 1–3 potentials that exhibit shapes difficult to fit with simple analytical forms. As implemented in the MCCC–MN program, the tabulated bonded potentials also come with a significant gain in computational efficiency.

■ ASSOCIATED CONTENT

S Supporting Information. Tables listing the numerical data for the vapor–liquid coexistence properties of the parametrization compounds (Table S1), the validation compounds (Table S2), and the *n*-hexane/*n*-hexatriacontane mixture (Table S3). The tabulated TraPPE–CG potentials for bonded and nonbonded interactions are provided as electronic files. This material is available free of charge via the Internet at <http://pubs.acs.org>.

■ AUTHOR INFORMATION

Corresponding Author

*E-mail: siepmann@umn.edu.

■ ACKNOWLEDGMENT

Financial support from the National Science Foundation (CBET-0756641) and a Graduate School Doctoral Dissertation Fellowship (K.A.M.) are gratefully acknowledged. Part of the computer resources was provided by the Minnesota Supercomputing Institute.

■ REFERENCES

- (1) Allen, M. P.; Tildesley, D. J. *Computer Simulation of Liquids*; Oxford University Press: New York, 1987.
- (2) Frenkel, D.; Smit, B. *Understanding Molecular Simulation: From Algorithms to Applications*; Academic Press: San Diego, CA, 2002.
- (3) McDonald, I. R. *Mol. Phys.* **1972**, *23*, 41–58.
- (4) Ryckaert, J. P.; Bellemans, A. *Chem. Phys. Lett.* **1975**, *30*, 123–125.
- (5) Müller-Plate, F. *Chem. Phys. Chem.* **2002**, *3*, 754–769.
- (6) Site, L. D.; Abrams, C. F.; Alavi, A.; Kremer, K. *Phys. Rev. Lett.* **2002**, *89*, 156103.

- (7) Sun, Q.; Faller, R. *Comput. Chem. Eng.* **2005**, *29*, 2380–2385.
- (8) Villa, E.; Balaeff, A.; Schulten, K. *Proc. Natl. Acad. Sci.* **2005**, *102*, 6783–6788.
- (9) Peter, C.; Kremer, K. *Soft Matter* **2009**, *5*, 4357–4366.
- (10) Siepmann, J. I. *NIST Spec. Pub.* **2001**, *975*, 110–112.
- (11) Reith, D.; Pütz, M.; Müller-Plathe, F. *J. Comput. Chem.* **2003**, *24*, 1624–1636.
- (12) Milano, G.; Müller-Plathe, F. *J. Phys. Chem. B* **2005**, *109*, 18609–18619.
- (13) Spyriouni, T.; Tzoumaneka, C.; Theodorou, D.; Müller-Plathe, F.; Milano, G. *Macromolecules* **2007**, *40*, 3876–3885.
- (14) Hansen, J. P.; McDonald, I. R. *Theory of Simple Liquids*, 3rd ed.; Academic Press: Burlington, MA, 2006.
- (15) Barker, J. A.; Henderson, D. *J. Chem. Phys.* **1967**, *47*, 4714.
- (16) Weeks, J. D.; Chandler, D.; Andersen, H. C. *J. Chem. Phys.* **1971**, *54*, 5237.
- (17) Jain, S.; Garde, S.; Kumar, S. K. *Ind. Eng. Chem. Res.* **2006**, *45*, 5614–5618.
- (18) Chan, E. R.; Striolo, A.; McCabe, C.; Cummings, P. T.; Glotzer, S. C. *J. Chem. Phys.* **2007**, *127*, 114102.
- (19) Hadley, K. R.; McCabe, C. *J. Phys. Chem. B* **2010**, *114*, 4590–4599.
- (20) Hadley, K. R.; McCabe, C. *J. Chem. Phys.* **2010**, *132*, 134505.
- (21) Izvekov, S.; Voth, G. A. *J. Phys. Chem. B* **2005**, *109*, 2469–2473.
- (22) Izvekov, S.; Swanson, J. M. J.; Voth, G. A. *J. Phys. Chem. B* **2008**, *112*, 4711–4724.
- (23) Wang, Y.; Noid, W. G.; Liu, P.; Voth, G. A. *Phys. Chem. Chem. Phys.* **2009**, *11*, 2002–2015.
- (24) Krishna, V.; Noid, W. G.; Voth, G. A. *J. Chem. Phys.* **2009**, *131*, 024103.
- (25) Marrink, S. J.; Risselada, H. J.; Yefimov, S.; Tieleman, D. P.; de Vries, A. H. *J. Phys. Chem. B* **2007**, *111*, 7812–7824.
- (26) Winger, M.; Trzesniak, D.; Baron, R.; van Gunsteren, W. F. *Phys. Chem. Chem. Phys.* **2009**, *11*, 1934–1941.
- (27) Winger, M.; Trzesniak, D.; Baron, R.; van Gunsteren, W. F. *Phys. Chem. Chem. Phys.* **2010**, *12*, 2254–2256.
- (28) Chiu, S.-W.; Scott, H. L.; Jakobsson, E. *J. Chem. Theory Comput.* **2010**, *6*, 851–868.
- (29) Shelley, J. C.; Shelley, M. Y.; Reeder, R. C.; Bandyopadhyay, S.; Klein, M. L. *J. Phys. Chem. B* **2001**, *105*, 4464–4470.
- (30) Shinoda, W.; DeVane, R.; Klein, M. L. *Mol. Simul.* **2007**, *33*, 27–36.
- (31) DeVane, R.; Shinoda, W.; Moore, P. B.; Klein, M. L. *J. Chem. Theory Comput.* **2009**, *5*, 2115–2124.
- (32) He, X. B.; Shinoda, W.; DeVane, R.; Klein, M. L. *Mol. Phys.* **2010**, *108*, 2007–2020.
- (33) Allen, E. C.; Rutledge, G. C. *J. Chem. Phys.* **2008**, *128*, 154115.
- (34) Allen, E. C.; Rutledge, G. C. *J. Chem. Phys.* **2009**, *130*, 034904.
- (35) Detcheverry, F. A.; Kang, H. M.; Daoulas, K. C.; Müller, M.; Nealey, P. F.; de Pablo, J. J. *Macromolecules* **2008**, *41*, 4989–5001.
- (36) Detcheverry, F. A.; Pike, D. Q.; Nagpal, U.; Nealey, P. F.; de Pablo, J. J. *Soft Matter* **2010**, *5*, 4858–4865.
- (37) Mognetti, B. M.; Virnau, P.; Yelash, L.; Paul, W.; Binder, K.; Müller, M.; MacDowell, L. G. *J. Chem. Phys.* **2009**, *130*, 044101.
- (38) Liew, C. C.; Mikami, M. *Chem. Phys. Lett.* **2003**, *368*, 346–351.
- (39) Martin, M. G.; Siepmann, J. I. *J. Chem. Phys.* **1998**, *102*, 2569–2577.
- (40) Martin, M. G.; Siepmann, J. I. *J. Phys. Chem. B* **1999**, *103*, 4508–4517.
- (41) Chen, B.; Potoff, J. J.; Siepmann, J. I. *J. Phys. Chem. B* **2001**, *105*, 3093–3104.
- (42) Stubbs, J. M.; Potoff, J. J.; Siepmann, J. I. *J. Phys. Chem. B* **2004**, *108*, 17596–17605.
- (43) Chen, B.; Siepmann, J. I. *J. Phys. Chem. B* **1999**, *103*, 5370–5379.
- (44) Wick, C. D.; Stubbs, J. M.; Rai, N.; Siepmann, J. I. *J. Phys. Chem. B* **2005**, *109*, 18974–18982.
- (45) Rai, N.; Siepmann, J. I. *J. Phys. Chem. B* **2007**, *111*, 10790–10799.
- (46) Chen, B.; Xing, J.; Siepmann, J. I. *J. Phys. Chem. B* **2000**, *104*, 2391–4201.
- (47) Chen, B. Phase Equilibria of Hydrocarbons, Alcohols, Water and their Mixtures. Ph.D. Thesis, University of Minnesota, 2001.
- (48) Wick, C. D.; Theodorou, D. N. *Macromolecules* **2004**, *37*, 7026–7033.
- (49) Wick, C. D.; Siepmann, J. I.; Theodorou, D. N. *J. Am. Chem. Soc.* **2005**, *127*, 12338–12342.
- (50) Rissanou, A. N.; Peristeras, L. D.; Economou, I. G. *Polymer* **2007**, *48*, 3883–3892.
- (51) Li, H.; Curro, J. G.; Wu, D. T.; Habenschuss, A. *Macromolecules* **2008**, *41*, 2694–2700.
- (52) Bernstein, J. *Polymorphism in Molecular Crystals*; Oxford University Press: New York, 2002.
- (53) Chen, B.; Siepmann, J. I.; Klein, M. *J. Am. Chem. Soc.* **2002**, *124*, 12232–12237.
- (54) Nellas, R. B.; Chen, B. *Phys. Chem. Chem. Phys.* **2008**, *10*, 506–514.
- (55) Rafferty, J. L.; Siepmann, J. I.; Schure, M. R. *Anal. Chem.* **2008**, *80*, 6214–6221.
- (56) Rai, N.; Wagner, A. J.; Ross, R. B.; Siepmann, J. I. *J. Chem. Theor. Comput.* **2008**, *4*, 136–144.
- (57) Kelkar, M. S.; Rafferty, J. L.; Siepmann, J. I.; Maginn, E. J. *Fluid Phase Equilib.* **2007**, *260*, 218–231.
- (58) Polyakov, P.; Rossinsky, E.; Wiegand, S. *J. Phys. Chem. B* **2009**, *113*, 13308–13312.
- (59) Dubbeldam, D.; Galvin, C. J.; Walton, K. S.; Ellis, D. E.; Snurr, R. Q. *J. Am. Chem. Soc.* **2008**, *130*, 10884–10885.
- (60) Jakobtorweihen, S.; Keil, F. J. *Mol. Simul.* **2009**, *35*, 90–99.
- (61) Dodd, L. R.; Boone, T. D.; Theodorou, D. N. *Mol. Phys.* **1993**, *78*, 961–966.
- (62) Wick, C. D.; Siepmann, J. I. *Macromolecules* **2000**, *33*, 7207–7218.
- (63) Monte Carlo for Complex Chemical Systems—Minnesota, Version 10.1, <http://www.chem.umn.edu/groups/siepmann/software.html>.
- (64) Siepmann, J. I.; Frenkel, D. *Mol. Phys.* **1992**, *75*, 59–70.
- (65) Frenkel, D.; Mooij, G. C. A. M.; Smit, B. *J. Phys.: Condens. Matter* **1992**, *4*, 3053–3076.
- (66) de Pablo, J. J.; Laso, M.; Siepmann, J. I.; Suter, U. W. *Mol. Phys.* **1993**, *80*, 55–63.
- (67) Vlucht, T. J. H.; Martin, M. G.; Smit, B.; Siepmann, J. I.; Krishna, R. *Mol. Phys.* **1998**, *94*, 727–733.
- (68) Panagiotopoulos, A. Z. *Mol. Phys.* **1987**, *61*, 813–826.
- (69) Panagiotopoulos, A. Z.; Quirke, N.; Stapleton, M.; Tildesley, D. J. *Mol. Phys.* **1988**, *63*, 527–545.
- (70) Rowlinson, J. S.; Widom, B. *Molecular Theory of Capillarity*; Oxford University Press: New York, 1989.
- (71) Rowlinson, J. S.; Swinton, F. L. *Liquids and Liquid Mixtures*; Butterworth: London, 1982.
- (72) Ben-Naim, A. *Statistical Thermodynamics for Chemists and Biochemists*; Plenum: New York, 1992.
- (73) Martin, M. G.; Siepmann, J. I. *Theor. Chem. Acc.* **1998**, *99*, 347–350.
- (74) Errington, J. R.; Panagiotopoulos, A. Z. *J. Phys. Chem. B* **1999**, *103*, 6314–6322.
- (75) Ungerer, P.; Beauvais, C.; Delhommelle, J.; Boutin, A.; Rousseau, B.; Fuchs, A. H. *J. Chem. Phys.* **2000**, *112*, 5499–5510.
- (76) Potoff, J. J.; Bernard-Brunel, D. A. *J. Phys. Chem. B* **2009**, *113*, 14725–14731.
- (77) Maitland, G. C.; Rigby, M.; Smith, E. B.; Wakeham, A. *Intermolecular Forces: Their Origin and Determination*; Pergamon Press: Oxford, UK, 1987.
- (78) Siepmann, J. I.; Karaborni, S.; Smit, B. *J. Am. Chem. Soc.* **1993**, *115*, 6454–6455.
- (79) Chen, B.; Martin, M. G.; Siepmann, J. I. *J. Phys. Chem. B* **1998**, *102*, 2578–2586.

- (80) Baron, R.; Trzesniak, D.; de Vries, A. H.; Elsener, A.; Marrink, S. J.; van Gunsteren, W. F. *Chem. Phys. Chem.* **2007**, *8*, 452–461.
- (81) Zhuravlev, N. D.; Martin, M. G.; Siepmann, J. I. *Fluid Phase Equilib.* **2002**, *202*, 307–324.
- (82) Anselme, M. J.; Gude, M.; Teja, A. S. *Fluid Phase Equilib.* **1990**, *57*, 317–326.
- (83) Siepmann, J. I.; Karaborni, S.; Smit, B. *Nature* **1993**, *365*, 330–332.
- (84) de Loos, T. W.; de Graaf, L. J.; de Swaan Arons, J. *Fluid Phase Equilib.* **1996**, *117*, 40–47.
- (85) Joyce, P. C.; Gordon, J.; Thies, M. C. *J. Chem. Eng. Data* **2000**, *45*, 424–427.
- (86) Ting, P. D.; Joyce, P. C.; Jog, P. K.; Chapman, W. G.; Thies, M. C. *Fluid Phase Equilib.* **2003**, *206*, 267–286.
- (87) Paricaud, P.; Galindo, A.; Jackson, G. *Ind. Eng. Chem. Res.* **2004**, *43*, 6871–6889.
- (88) Peng, Y.; Goff, K. D.; dos Ramos, M. C.; McCabe, C. *Ind. Eng. Chem. Res.* **2010**, *49*, 1378–1394.
- (89) de Pablo, J. J.; Laso, M.; Suter, U. W. *Macromolecules* **1993**, *26*, 6180–6183.
- (90) Spyriouni, T.; Economou, I. G.; Theodorou, D. N. *J. Am. Chem. Soc.* **1999**, *121*, 3407–3413.